

ReFRM3D: A Radiomics-enhanced Fused Residual Multiparametric 3D Network with Multi-Scale Feature Fusion for Glioma Characterization

Md. Abdur Rahman^{1,2}, Mohaimenul Azam Khan Raiaan^{1,2,3,*}, Arefin Ittesafun Abian^{1,2}, Yan Zhang⁴, Mirjam Jonkman⁴, Sami Azam^{4,*}

¹Applied Artificial Intelligence and Intelligent Systems (AAIINS) Laboratory, Dhaka 1217, Bangladesh

²Department of Computer Science and Engineering, United International University, Dhaka, 1212, Bangladesh

³Department of Data Science and Artificial Intelligence, Monash University, Clayton, VIC, 3153, Australia

⁴Faculty of Science and Technology, Charles Darwin University, Darwin, 0909, Australia

*Corresponding Authors: mraiaan191228@bscse.uui.ac.bd; sami.azam@cdu.edu.au

Abstract

Gliomas are among the most aggressive cancers, characterized by high mortality rates and complex diagnostic processes. Existing studies on glioma diagnosis and classification often describe issues such as high variability in imaging data, inadequate optimization of computational resources, and inefficient segmentation and classification of gliomas. To address these challenges, we propose novel techniques utilizing multi-parametric MRI data to enhance tumor segmentation and classification efficiency. Our work introduces the first-ever radiomics-enhanced fused residual multiparametric 3D network (ReFRM3D) for brain tumor characterization, which is based on a 3D U-Net architecture and features multi-scale feature fusion, hybrid upsampling, and an extended residual skip mechanism. Additionally, we propose a multi-feature tumor marker-based classifier that leverages radiomic features extracted from the segmented regions. Experimental results demonstrate significant improvements in segmentation performance across the BraTS2019, BraTS2020, and BraTS2021 datasets, achieving high Dice Similarity Coefficients (DSC) of 94.04%, 92.68%, and 93.64% for whole tumor (WT), enhancing tumor (ET), and tumor core (TC) respectively in BraTS2019; 94.09%, 92.91%, and 93.84% in BraTS2020; and 93.70%, 90.36%, and 92.13% in BraTS2021.

Keywords: Feature Map, Glioma Characterization, Multiparametric MRI, Multi-scale Feature Fusion, Radiomics

1 Introduction

Brain tumors are among the most dangerous types of cancer and are the second most common childhood cancer. Meningiomas, pituitary adenomas, and gliomas are the three most common types of primary brain tumors. Studies have shown that in 2023, approximately 19,000 people were expected to die from malignant brain tumors [Ostrom et al. \(2022\)](#); [Siegel et al. \(2023\)](#). Every year, six cases of gliomas are detected per 100,000 people in the United States. These tumors range from low-grade pilocytic astrocytomas to highly malignant glioblastomas, with significant variations in both aggressiveness and prognosis. Glioblastomas, the malignant brain tumors with the highest incidence, account for 14.9% of all primary brain tumors and 55.4% of gliomas [Ostrom et al. \(2022\)](#).

Medical imaging is used by doctors to assess patient conditions in order to make clinical diagnoses. Medical image segmentation and classification have the potential to contribute to affordable healthcare through the automatic identification of anatomical structures and other regions of interest

[Mazurowski et al. \(2023\)](#); [Esteva et al. \(2019\)](#); [Nazir et al. \(2023\)](#); [Koetzier et al. \(2023\)](#). Clinicians are increasingly using computer-aided diagnosis (CAD) to identify abnormal structures. Segmentation and classification with the aim to visualize changes in the diseased or anatomical structure of the images are crucial components of CAD [Dhar et al. \(2023\)](#); [Balraj et al. \(2024\)](#). Developing CAD systems integrated with ML or deep learning (DL) to segment or classify gliomas could aid clinicians in detecting tumors at an initial stage [Usha et al. \(2024\)](#). Researchers used model-driven methods (adaptable models [Zhang and Metaxas \(2024\)](#), statistical structural models [Fernando and Tsokos \(2023\)](#), and active contours [Chen et al. \(2019\)](#)) for medical image segmentation before deep learning became widely used. These methods usually require human interaction. On the other hand, automating these procedures to improve accuracy and efficiency is the goal of CAD models.

In recent years, different methodologies for CAD systems for brain tumors have been presented, including 2D and 3D models with various kinds of objectives [Salman et al. \(2024\)](#);

Jyothi and Singh (2023); Fernando and Tsokos (2023). To classify tumors, several 2D models have been combined with encoder-decoders, and CNNs are employed for segmentation. However, constructing a 2D model is insufficient to effectively categorize or segment images Hesamian et al. (2019). Utilizing 3D models is more effective because they have sophisticated features and more precisely represent temporal and spatial relationships—two things that are essential in medical imaging. However, because 3D imaging requires an enormous amount of processing power, working with it can be difficult. Scans of a number of slices need to be handled during the process, requiring a large amount of computing and storage capacity, particularly when working with massive datasets or multi-modal images Azad et al. (2024). Furthermore, efficient processing of the depth information and temporal-spatial relationships in these 3D models frequently calls for complex algorithms. Suitable compression algorithms could provide a way to reduce this problem without the loss of vital information.

Accurately delineating the structures within the brain remains a major challenge and variability or optimization of computational resources have often not been taken into account. Previous researchers have carried out multi-label segmentation and classification integrated with encoder-decoders. We have, however, addressed several shortcomings of the previous research. The major contributions of our study are as follows:

- A novel approach for isolating and cropping brain regions from 3D MRI scans using intensity thresholding and connected component analysis is introduced. The approach minimizes computational load while maintaining precise delineation of brain structures and enhancing ROI identification for tumor localization.
- A voxel intensity standardization technique is developed that reduces imaging variability across diverse MRI datasets, particularly addressing multi-grade glioma data (i.e., HGG and LGG). This ensures uniformity in neuroimaging data analysis across different tumor grades.
- An efficient data processing technique is integrated for 3D volumes that optimizes the input format, reduces computational overhead and enables training efficiency without compromising performance.
- To enhance multi-scale feature fusion, improve localization, and reduce interpolation artifacts in tumor segmentation, an extended 3D U-Net is proposed with augmented Fused Multi-scale Feature Fusion, Hybrid Upsampling, Residual Integration, and the Residual Skip Mechanism.
- A set of radiomics features is combined with segmentation-based features, generating a multi-dimensional feature representation that enhances tumor

classification and provides a detailed understanding of tumor morphology and structure.

The rest of the paper is organized as follows: Section 2 reviews related works. Section 3 describes the methodology, including preprocessing steps, segmentation model, and classifier architecture. Section 4 presents the analysis of segmentation and classification results, ablation studies, and comparisons with existing methods. Sections 5, and 6 discuss the findings, limitations, and future work directions, followed by the conclusion in Section 7, which summarizes the main contributions.

2 Related Works

Segmentation Architectures. The expected survival time of the patient, treatment planning, and tumor development evaluation are all directly impacted by the early and precise detection of the grade of brain tumor. Computer-aided diagnosis (CAD) may assist clinicians in classifying and detecting diseases at an early stage. Brain tumor segmentation can be helpful in diagnosis, tumor measurement, treatment planning, prediction of growth, and overall prognosis. Recent advancements in glioma segmentation have focused on optimizing feature reuse, multi-scale learning, and contextual information extraction. A range of studies Zhang et al. (2021a); Zhou et al. (2020, 2021); Ding et al. (2020); Li et al. (2019) utilize dense connectivity and feature fusion techniques to enhance segmentation performance. These architectures aim to improve feature flow across multiple scales, ensuring that both low and high-level information is effectively captured. For instance, Zhang et al. Zhang et al. (2021a) integrate multi-view 2D-CNN outputs with fused modalities to better represent spatial features. Similarly, some works Zhou et al. (2020, 2021) employ dense connectivity with atrous convolutions to enable better multi-scale learning and improve contextual feature extraction. Similarly, Ding et al. Ding et al. (2020) introduce adaptive fusion blocks, which preserve essential low-level and high-level features. Li et al. Li et al. (2019) incorporate inception modules to enable the model to capture diverse features across multiple scales which improves both local and global tumor representation. Complementing these approaches, dual-path networks Tong and Wang (2023); Jiang et al. (2021) focus on refining tumor boundary detection by addressing class-specific learning. Tong et al. Tong and Wang (2023) emphasize global and local feature separation, while Jiang et al. Jiang et al. (2021) enhance edge detection through dual-stream decoders that better delineate tumor boundaries. Attention mechanisms have also been widely explored to improve tumor feature extraction, particularly for subtle and difficult-to-segment areas. Liu et al. Liu et al. (2023b) utilize attention mechanisms that focus on tumor regions, ensuring finer segmentation in challenging areas. In

another study Liu et al. (2023a), this idea is extended by applying multi-scale attention to capture both large and fine tumor features. Similarly, Ullah et al. Ullah et al. (2022) adopt a cascade approach with progressive refinement to improve segmentation accuracy over multiple stages. Zhong et al. Zhong et al. (2020) introduce window-modulated attention targeting particularly difficult tumor areas where traditional methods struggle.

Multi-Modal Data Fusion. The integration of multi-modal MRI data has been essential for capturing tumor heterogeneity and enhancing segmentation performance. Several studies Barzegar and Jamzad (2021); Isensee et al. (2021); Xue et al. (2020); Xu et al. (2022); Sun et al. (2024) focus on multi-modal fusion to improve tumor boundary detection, while others Ranjbarzadeh et al. (2021); Guan et al. (2022); Li et al. (2022); Li and Guo (2024) emphasize radiomic feature extraction and preprocessing strategies to refine segmentation results. For example, Barzegar and Jamzad (2021) employ probabilistic graph-based voxel label fusion, integrating prior atlases with target image information to improve voxel-wise label assignment. Isensee et al. (2021) enhance nnU-Net through dataset-specific post-processing and ensemble strategies tailored for glioma segmentation tasks. Similarly, Xue et al. (2020) introduce a hypergraph membrane system for multi-modal ensemble learning to capture complex tumor structures across various MRI sequences. Xu et al. (2022) also focus on inter-slice dependencies by using corner attention modules which improves the handling of multi-slice spatial relationships in 3D MRI volumes. On the other hand, Sun et al. (2024) integrate statistical and visual feature extraction by combining radiomic features with deep learning techniques to classify glioma subtypes. Additionally, works such as Ranjbarzadeh et al. (2021); Guan et al. (2022); Li et al. (2022) incorporate advanced radiomic analysis and preprocessing techniques to further boost segmentation accuracy. Ranjbarzadeh et al. (2021) apply cascade CNNs with a distance-wise attention mechanism to refine segmentation boundaries. Guan et al. (2022) use Squeeze-and-Excite modules to enhance feature extraction and channel-wise attention in multi-modal networks.

Optimization Strategies. To address the class imbalance and improve segmentation performance, various studies have proposed customized loss functions and optimized training strategies. Several studies Domadia et al. (2024); Li and Guo (2024); Zhang et al. (2021b); Zhou et al. (2020); Zhong et al. (2020) introduce specialized loss functions, while others Liu et al. (2023a); Barzegar and Jamzad (2021) incorporate hybrid optimization techniques to stabilize training and refine boundary precision. For example, Domadia et al. (2024) combine focal Tversky and generalized Dice loss functions to balance the influence of underrepresented classes. Zhang et al. (2021b) propose a multi-scale mesh aggregation network that aggregates at different scales. Li and Guo (2024) use

multi-task loss functions that link segmentation and radiomic classification enabling unified optimization for the simultaneous learning of both tasks. Zhou et al. (2020) employ a Dice-Cross-Entropy loss to address the class imbalance and improve model robustness to data variations. Further, confidence-weighted label propagation Zhong et al. (2020) stabilizes training by adjusting label propagation based on predicted confidence. Similarly, Barzegar and Jamzad (2021) utilize confidence-weighted label propagation to stabilize the model’s learning in challenging regions. On the other hand, Liu et al. (2023a) apply hierarchical convolutions using different convolution strategies at various scales to optimize training and improve segmentation accuracy.

Computational Efficiency. In high-volume glioma segmentation, computational efficiency is a critical challenge, especially when handling memory and resource constraints. Several studies address this challenge by proposing lightweight architectures that reduce model complexity while maintaining high performance. For example, Isensee et al. (2021) streamline the nnU-Net framework by simplifying its structure, and reducing the depth of the network. Similarly, Liu et al. (2023a) optimize convolutional operations by replacing traditional convolutions with hierarchical decoupled convolutions. To further address resource limitations, Zhou et al. (2020) adopt ShuffleNetV2 encoders which reduce computational complexity while retaining effective feature extraction. Xu et al. (2022) take a different approach by incorporating modular attention mechanisms. It enables the model to scale effectively with limited memory. Similarly, Xue et al. (2020) enhance computational efficiency through multi-modal data fusion and ensemble learning techniques by reducing redundant operations.

Building on the findings from related works, several key gaps remain that require further investigation. For example, it is unclear whether isolating brain structures before segmentation significantly improves accuracy or if fewer slices can provide sufficient information without processing the entire image volume. Additionally, the value of integrating multi-modal MRI data compared to single-modal approaches in enhancing tumor delineation remains to be fully understood. Lastly, it is worth questioning whether current tumor marker classifications are sufficient or if additional markers are necessary for comprehensive glioma analysis. To explore these issues, we define the following research questions (RQs) to guide advancements in glioma segmentation and classification:

- **RQ1:** Despite numerous studies that do not isolate and crop brain regions, is it essential to investigate the accurate delineation of brain structures?
- **RQ2:** Is it necessary to perform the segmentation process on the entire slice range, or does segmentation using a reduced slice count provide sufficient value?

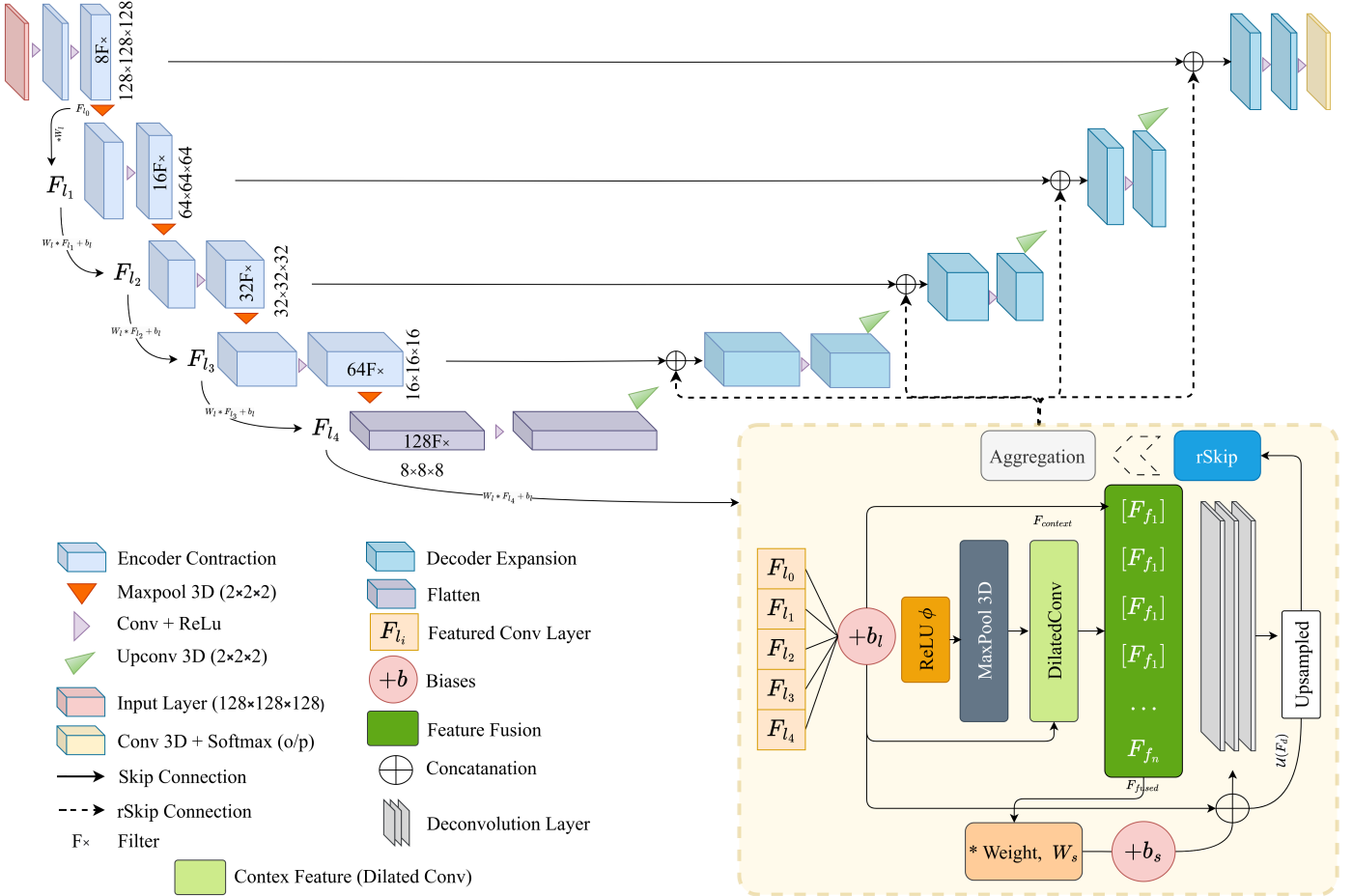


Figure 1: Overview of the proposed glioma segmentation framework. The expansion layers mirror the contraction layers in size and filters.

- **RQ3:** 3D segmentation models often face resource exhaustion problems due to the high data volume. Can these issues be effectively addressed?
- **RQ4:** Can integrating multi-modal MRI data (e.g., Flair, T1ce, and T2) into a unified segmentation framework improve the accuracy and reliability of tumor delineation compared to single-modal approaches?
- **RQ5:** Is the classification of different tumor markers sufficient, or are additional markers or classifications needed for a comprehensive analysis?

3 Methodology

The proposed ReFRM3D model combines several key components to address the challenges in glioma segmentation and classification. This includes a preprocessing pipeline for brain region isolation, voxel intensity standardization, and region of interest (ROI) identification. We introduce a custom 3D U-Net architecture with novel modules for accurate

tumor segmentation. Finally, we develop a multi-feature tumor marker-based classifier that utilizes radiomic features extracted from the segmented regions. Figure 1 illustrates the overall proposed segmentation framework. The details of each component are discussed in the following sections.

3.1 Datasets

For this research, we used three benchmark datasets from the Brain Tumor Segmentation (BraTS) challenge series: BraTS2019, BraTS2020, and BraTS2021. All datasets provide 3D multi-parametric MRI (mpMRI) scans in neuroimaging data format (.nii) for brain tumor segmentation in various MRI sequences and manual segmentations Menze et al. (2014); Bakas et al. (2017, 2018); Baid et al. (2021). The detailed distribution of the leveraged datasets is given in Table 1.

BraTS2019 dataset. BraTS2019 dataset comprises 3D mpMRI scans in NIFTI format from 626 patients diagnosed with gliomas, including both high-grade glioblastomas

Table 1: Dataset distribution. The *Goal* column provides information on whether the respective dataset was used only for evaluation or for both training and evaluation.

| Dataset | Training | Testing | Validation | Patients | Type | Goal |
|-----------|----------|---------|------------|----------|--------|------------------------------------------------------|
| BraTS2019 | 335 | 166 | 125 | 626 | 3D MRI | Evaluation: Segmentation & Classification |
| BraTS2020 | 369 | 166 | 125 | 660 | 3D MRI | Evaluation: Segmentation & Classification |
| BraTS2021 | 1251 | 570 | 219 | 2040 | 3D MRI | Training + Evaluation: Segmentation & Classification |

(GBM, grade 4) and lower-grade gliomas (LGG, grades 2 and 3). The dataset featured four MRI sequences: T1-weighted (T1), contrast-enhanced or post-contrast T1-weighted (T1gd/T1ce), T2-weighted (T2), and T2-Flair (Flair). Preprocessing steps for this dataset included co-registering the images to the SRI24 anatomical template, re-sampling to a uniform voxel size of 1 mm³, and applying skull-stripping to remove non-brain tissues. Manual segmentations for three key tumor sub-regions: the enhancing tumor (ET), tumor core (TC), and whole tumor (WT) were provided by neuroradiologists.

BraTS2020 dataset. The BraTS2020 dataset was built on the previous year’s dataset, with 660 glioma cases. The preprocessing pipeline mirrored BraTS2019 maintained four mpMRI sequences (T1, T1Gd, T2, and Flair), while segmentation tasks focused on the ET, TC, and WT sub-regions.

BraTS2021 dataset. BraTS2021 introduced an expansion featuring 2040 patients and a new radiogenomic classification task to predict the MGMT promoter methylation status in glioblastoma patients. This dataset includes the same MRI sequences as prior versions and a binary label for the radiogenomic task all provided in NIfTI format.

It is worth noting that T1gd/T1ce is the post-contrast/contrast-enhanced form of T1-weighted modality, thus in our experiment, we have not considered the T1 sequence, but rather considered the T1gd/T1ce sequence along with T2, and Flair.

3.2 Preprocessing

The datasets were preprocessed by converting 3D NIfTI files into .npy format to facilitate faster and more resource-efficient training while ensuring no data loss. This allowed for efficient input handling and better optimization during model training. The images were resized to 128×128×128 with three channels (i.e., Flair, T1ce/T1gd, T2). The following sections detail the preprocessing steps for optimizing MRI data, including brain region isolation, voxel intensity standardization, and slice range selection. The proposed steps are briefed in Algorithm 1.

3.2.1 Brain Region Isolation and Cropping

The isolation of the brain region from 3D MRI data is an essential preprocessing step for computational efficiency. In traditional methods, which involve selecting a fixed rectangular

Algorithm 1 Data Preprocessing

- 1: **Input:** 3D MRI Volumes $V = \{v_1, \dots, v_n\}$, Segmentation Masks $S = \{s_1, \dots, s_n\}$
 - 2: **Key Parameters:** Intensity Threshold T_i , Margin δ , Covariance Matrix Q , Mean Intensity μ , Std. Dev. σ , Z-score Z
 - 3: **for all** $v \in V$ **do**
 - 4: $T_i \leftarrow \text{percentile}(v, 99)$
 - 5: $M \leftarrow \text{binary_mask}(v, T_i)$
 - 6: $X \leftarrow \text{connected_components}(M)$
 - 7: $Q \leftarrow \text{covariance_matrix}(X)$
 - 8: $v_{\text{cropped}} \leftarrow \text{crop_region}(v, Q, \delta)$
 - 9: **end for**
 - 10: $V_{\text{cropped}} \leftarrow \{v_{\text{cropped}_i} \mid i = 1, \dots, n\}$
 - 11: **for all** $v_{\text{cropped}} \in V_{\text{cropped}}$ **do**
 - 12: $\mu, \sigma \leftarrow \text{mean_std}(v_{\text{cropped}})$
 - 13: $Z \leftarrow \text{normalize}(v_{\text{cropped}}, \mu, \sigma)$
 - 14: **end for**
 - 15: $V_{\text{normalized}} \leftarrow \{Z_i \mid i = 1, \dots, n\}$
 - 16: **for all** $s \in S$ **do**
 - 17: $S_{\text{start}} \leftarrow \min\{z \mid \max(s_z) > 0\}$
 - 18: $S_{\text{end}} \leftarrow \max\{z \mid \max(s_z) > 0\}$
 - 19: $v_{\text{sliced}} \leftarrow \text{slice_volume}(v_{\text{normalized}}, S_{\text{start}}, S_{\text{end}})$
 - 20: **end for**
 - 21: $V_{\text{preprocessed}} \leftarrow \{v_{\text{sliced}_i} \mid i = 1, \dots, n\}$
 - 22: **for all** $v_{\text{preprocessed}} \in V_{\text{preprocessed}}$ **do**
 - 23: $\text{Vol}[i] \leftarrow \text{reshape}(v_{\text{preprocessed}}, 128^3)$
 - 24: $\text{Vol}_{\text{data}}[i] \leftarrow \text{to_numpy}(\text{Vol}[i])$
 - 25: **end for**
 - 26: **Output:** Processed Data, $\text{Vol}_{\text{data}}[i]$
-

region from MRI images, there is a significant risk of including non-brain regions or excluding critical brain areas from the scans due to the variable position of brain regions within the volume. To overcome these challenges, we introduce a novel method that automates the isolation the brain region, preserving all relevant information by taking into account the multi-planar nature of the MRI data (axial, coronal, and sagittal planes) and the variability in slice positioning.

First, the intensity values are normalized across different scans to ensure consistency. An initial binary mask M is then generated using intensity thresholding, where the threshold T is set at the 99th percentile of the voxel intensity distribution V . It is calculated as shown in Equation (1):

$$M(i, j, k) = \begin{cases} 1 & \text{if } V(i, j, k) > T \\ 0 & \text{otherwise} \end{cases} \quad (1)$$

where $M(i, j, k)$ represents the presence (1) or absence (0) of brain tissue at voxel (i, j, k) . We use this binary mask as an initial approximation of the brain region. Next, to refine this mask and remove potential high-intensity artifacts, we perform connected component analysis and retain only the largest connected component, which we assume to represent the brain region.

Once the isolation of the brain component is completed, we extract the voxel coordinates in this region as $X = \{(x_i, y_i, z_i)\}$. To define the brain's bounding box, we perform Principal Component Analysis (PCA) on X and compute the covariance matrix \mathbf{C} :

$$\mathbf{C} = \frac{1}{n} \sum_{i=1}^n (X_i - \bar{X})(X_i - \bar{X})^T \quad (2)$$

where \bar{X} is the mean of the voxel coordinates. The eigenvectors Q_j of \mathbf{C} indicate the principal axes of the brain. To determine the bounding box, we calculate the minimum and maximum extents of the brain region along the principal axes by projecting the coordinates of each brain voxel onto the eigenvectors associated with each principal direction:

$$\begin{aligned} x_{\min} &= \min_{i=1, \dots, n} (X_i \cdot Q_x), & x_{\max} &= \max_{i=1, \dots, n} (X_i \cdot Q_x), \\ y_{\min} &= \min_{i=1, \dots, n} (X_i \cdot Q_y), & y_{\max} &= \max_{i=1, \dots, n} (X_i \cdot Q_y), \\ z_{\min} &= \min_{i=1, \dots, n} (X_i \cdot Q_z), & z_{\max} &= \max_{i=1, \dots, n} (X_i \cdot Q_z) \end{aligned} \quad (3)$$

where Q_x , Q_y , and Q_z are the eigenvectors of the covariance matrix along each axis. Each eigenvector represents a principal direction in 3D space that aligns with the shape of the brain region. By projecting the voxel coordinates onto these eigenvectors, we identify the furthest extents of the brain region in each principal direction. Finally, to account for anatomical variability, we add a margin to these bounds, calculated based on the standard deviations of the voxel coordinates along each axis. This margin-adjusted bounding box ensures that the brain region is accurately cropped without including irrelevant non-brain regions.

3.2.2 Standardizing Voxel Intensities

After brain region isolation and cropping, Z-score normalization is applied to standardize voxel intensity values across the MRI volumes. This step addresses intensity variations arising from differences in MRI acquisition sequences, such as T1-weighted (T1), Post-contrast/Enhanced T1-weighted (T1ce/gd), T2-weighted (T2), and Fluid-Attenuated Inversion Recovery (Flair). To perform Z-score normalization, we use the previously obtained brain region mask to focus intensity calculations on the relevant anatomical structures.

First, the voxel intensities within the segmented brain region are extracted, and statistical metrics such as the mean μ and standard deviation σ are computed, as shown in Equations (4), and (5):

$$\mu = \frac{1}{N} \sum_{i=1}^N v_i \quad (4)$$

$$\sigma = \sqrt{\frac{1}{N} \sum_{i=1}^N (v_i - \mu)^2} \quad (5)$$

where v_i represents each voxel's intensity value, and N is the total number of voxels within the brain region.

Following this, Z-score normalization is performed to center voxel intensities around a mean of zero and scale them to have a standard deviation of one. For each voxel intensity v_{ijk} , the normalized value Z_{ijk} is computed as shown in Equation (6). Figure 2 visually compares the original and normalized MRI intensity distributions.

$$Z_{ijk} = \frac{v_{ijk} - \mu}{\sigma} \quad (6)$$

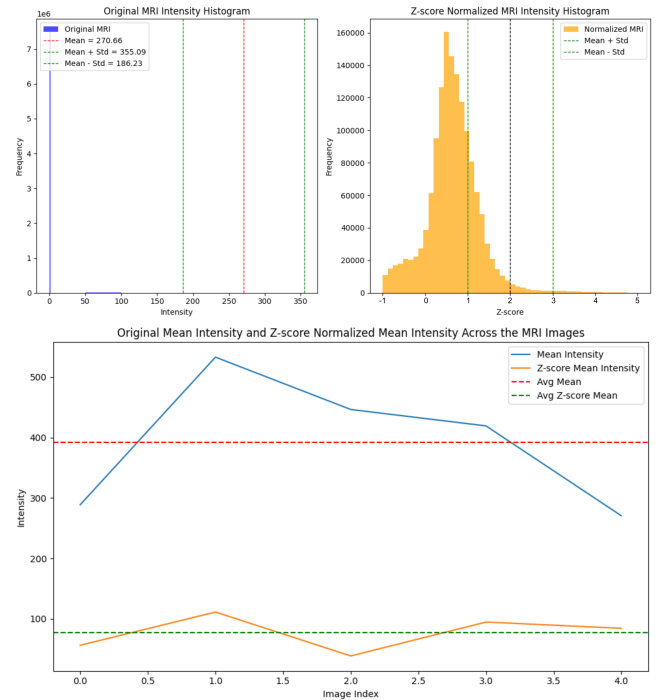


Figure 2: Visualization of histograms of original and Z-score normalized intensity distributions with intensity comparison across multiple MRI scans.

3.2.3 Slice Range Selection

Our analysis found that certain MRI volume slices do not contain relevant tumor regions and including them results in

unnecessary resource consumption and may introduce noise. We therefore developed a preprocessing method that isolates tumor-containing MRI slices, reducing computational load and enhancing segmentation accuracy by focusing the model’s training and inference on relevant slices.

In our approach, we first identify the tumor-containing slices by checking if the segmentation mask for each slice contains any non-zero values. For a slice s in the segmentation mask S , the tumor-containing slices are defined as those where the maximum intensity exceeds zero. The start and end slices of the tumor region are computed as:

$$S_{\text{start}} = \min\{s \mid \max(S_s) > 0\} \quad (7)$$

$$S_{\text{end}} = \max\{s \mid \max(S_s) > 0\} \quad (8)$$

where S_{start} and S_{end} represent the indices of the first and last slices containing tumor regions, respectively.

We then restrict the depth dimension D from the original volume size (D, H, W) to the range $[S_{\text{start}}, S_{\text{end}}]$ which results in a reduced size of $(S_{\text{end}} - S_{\text{start}} + 1, H, W)$. This focuses the model on tumor-containing slices while optimizing computational efficiency. Figure 3 illustrates the selected slice ranges for this experiment. Note that experimenting on the selected slices rather than the whole slices of each (3D data) volume did not cause any performance loss, but rather helped minimize computational resources.

3.3 Segmentation Model

In this section, we detail the proposed segmentation model for glioma segmentation, starting with the base 3D U-Net architecture. The proposed segmentation algorithm is outlined in Algorithm 2.

3.3.1 Base Model

The foundation of our model is based on the 3D U-Net architecture by Çiçek et al. (2016). The base architecture uses an encoder-decoder structure that captures spatial context. The input MRI volume, $X \in \mathbb{R}^{D \times H \times W}$, represents the three spatial dimensions: depth D , height H , and width W . The network progressively downsamples the input volume through convolutional and pooling operations. Each convolutional layer is followed by a non-linear activation function, $\phi(\cdot)$, and a downsampling operation, \mathcal{P} . After passing through l layers of convolution and pooling, the encoded feature map F_l is defined as:

$$F_l = \mathcal{P}(\phi(W_l * X + b_l)) \quad (9)$$

where $W_l \in \mathbb{R}^{C_l \times C_{l-1} \times k \times k}$ and $b_l \in \mathbb{R}^{C_l}$ are the learnable weights and biases for the l^{th} layer, C_l is the number of channels in the l^{th} layer, and $*$ denotes the convolution operation. The pooling operation \mathcal{P} is typically represented by max pooling, which reduces the spatial dimensions while preserving important features.

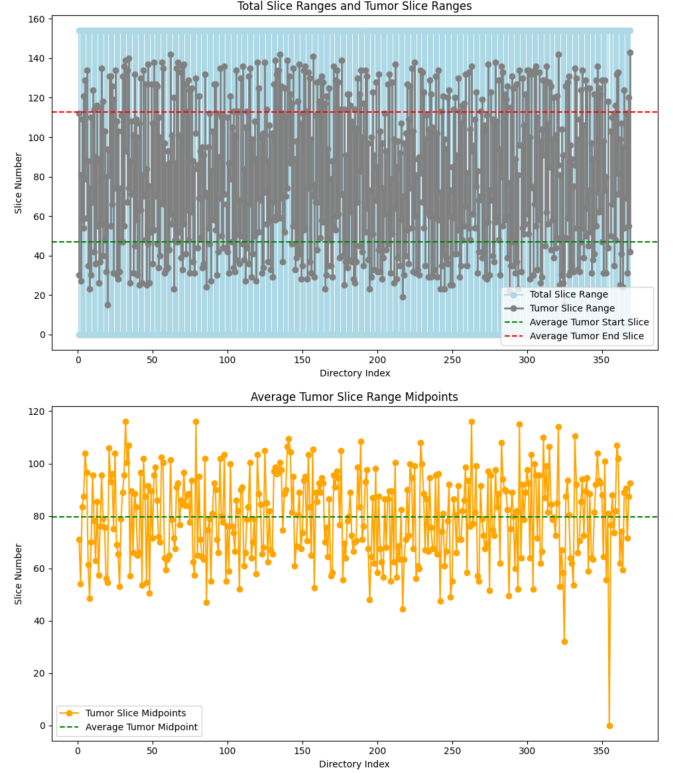


Figure 3: Visualization of total slice ranges and tumor slice distribution with midpoints: the average tumor start-slice is 46, ending at 113, with a total slice count of approximately 155 per volume.

Algorithm 2 Proposed Segmentation Model

- 1: **Input:** Preprocessed 3D MRI Volumes $V_{\text{data}} = \{v_{\text{preprocessed}_1}, \dots, v_{\text{preprocessed}_n}\}$
 - 2: **Key Parameters:** $F_{\text{context}}, F_{\text{fused}}, F_d, F_{\text{upsampled}}, F_{\text{res}}, F_{\text{aggr}}$
 - 3: **for all** $v \in V_{\text{data}}$ **do**
 - 4: $F_l \leftarrow \text{conv_layer}(v)$
 - 5: **for** $l = 1$ to L_{encoder} **do**
 - 6: $F_l \leftarrow \mathcal{P}(\phi(W_l * F_{l-1} + b_l))$
 - 7: **end for**
 - 8: $F_{\text{context}} \leftarrow \text{dilated_conv}(F_l)$
 - 9: $F_{\text{fused}} \leftarrow \sum_{s=1}^S W_s * F_s + b_s$
 - 10: $F_d \leftarrow \text{deconvolution_layer}(F_{\text{fused}})$
 - 11: **for** $d = 1$ to L_{decoder} **do**
 - 12: $F_d \leftarrow \mathcal{U}(\phi(W_d * F_{d-1} + b_d))$
 - 13: **end for**
 - 14: $F_{\text{upsampled}} \leftarrow \mathcal{U}(F_d)$
 - 15: $F_{\text{res}} \leftarrow F_{\text{upsampled}} + F_e$
 - 16: $F_{\text{o/p}} \leftarrow \phi(W_{\text{res}} * F_{\text{res}} + b_{\text{res}})$
 - 17: $F_{\text{rskip}} \leftarrow F_d + \mathcal{R}(F_e)$
 - 18: $F_{\text{aggr}} \leftarrow \text{aggregate}(F_{\text{rskip}})$
 - 19: **end for**
 - 20: **Output:** Aggregated Features, F_{aggr}
-

The decoder path mirrors the encoder by applying up-sampling operations \mathcal{U} to recover spatial resolution. This is achieved through deconvolution layers, which perform the reverse operation of convolution. The final segmentation map $\hat{Y}_{F_d} \in \mathbb{R}^{D \times H \times W}$ is obtained through:

$$\hat{Y}_{F_d} = \mathcal{U}(\phi(W_d * F_{d-1} + b_d)) \quad (10)$$

where $W_d \in \mathbb{R}^{C_d \times C_{d-1} \times k \times k}$ and $b_d \in \mathbb{R}^{C_d}$ are the learnable weights and biases for the d^{th} layer, and $*$ denotes the convolution operation. F_d represents the feature map generated after each deconvolution operation.

3.3.2 Context Pathway

While the base model captures local features, we found that it fails to gather sufficient global context. We introduce a context pathway that addresses this by expanding the receptive field through dilated convolutions. This enables the model to integrate larger spatial contexts without downsampling. For an input feature map $F \in \mathbb{R}^{C \times D \times H \times W}$, the dilated convolution operation with dilation rate r is defined as:

$$F_{\text{dilated}} = W_{\text{dilated}} F + b_{\text{dilated}} \quad (11)$$

where $W_{\text{dilated}} \in \mathbb{R}^{C_{\text{out}} \times C_{\text{in}} \times k \times k}$ and $b_{\text{dilated}} \in \mathbb{R}^{C_{\text{out}}}$ are the learnable weights and biases, respectively, and \cdot denotes the dilated convolution operation. The dilation rate r controls the spacing between kernel elements, thus expanding the receptive field while maintaining the resolution of the feature map. The output is then passed through a non-linear activation function, $\phi(\cdot)$, to introduce non-linearity:

$$F_{\text{dilated}} = \phi(F_{\text{dilated}}) \quad (12)$$

3.3.3 Multi-scale Feature Fusion

In addition to the context pathway, we implement a fused multi-scale feature fusion (FMFF) mechanism to capture both fine-grained local details and broad contextual information. This approach involves extracting feature maps at multiple scales and combining them to form a richer feature representation. Each scale produces a feature map $F_s \in \mathbb{R}^{C \times D_s \times H_s \times W_s}$, where s denotes the scale level and D_s, H_s, W_s are the spatial dimensions at that scale. To align the feature maps across scales, we apply a learnable convolution operation to each feature map:

$$\tilde{F}_s = W_s * F_s + b_s \quad (13)$$

where $W_s \in \mathbb{R}^{C_{\text{out}} \times C_{\text{in}} \times k \times k}$ and $b_s \in \mathbb{R}^{C_{\text{out}}}$ are the learnable weights and biases for the s^{th} scale, and $*$ denotes the convolution operation. After alignment, the fused feature maps from different scales are aggregated as defined:

$$F_{\text{fused}} = \sum_{s=1}^S \tilde{F}_s \quad (14)$$

where S represents the total number of scales considered. The fusion process ensures that the model leverages both local and global features and enriches the feature representation for structures of varying sizes.

3.3.4 Hybrid Upsampling and Residual Integration

It is observed that while the base model’s decoder employs upsampling operations to recover spatial resolution, this also leads to a loss of fine-grained details. We introduce a Hybrid Upsampling and Residual Integration (HUSR) strategy to address this limitation. This mechanism combines traditional upsampling with residual connections and allows us to preserve high-resolution details while reconstructing the segmentation map more effectively. At each decoding layer, we first apply an upsampling operation to the feature map $F_d \in \mathbb{R}^{C \times D \times H \times W}$ using transposed convolutions:

$$F_{\text{upsampled}} = \mathcal{U}(F_d) \quad (15)$$

where \mathcal{U} denotes the upsampling operation. To retain high-resolution details that might be lost during the upsampling process, we integrate residual connections. Specifically, we add the corresponding encoder feature map $F_e \in \mathbb{R}^{C \times D_e \times H_e \times W_e}$ to the upsampled feature map:

$$F_{\text{residual}} = F_{\text{upsampled}} + F_e \quad (16)$$

This residual connection allows us to preserve spatial information from the encoder, ensuring that high-resolution features—such as small tumor regions—are effectively maintained throughout the decoding process. Following this, a convolutional layer is applied to refine the feature map:

$$F_{\text{output}} = \phi(W_{\text{residual}} * F_{\text{residual}} + b_{\text{residual}}) \quad (17)$$

where W_{residual} and b_{residual} are the learnable weights and biases of the residual layer, and $*$ represents the convolution operation. The hybrid upsampling and residual integration approach enhances our model’s ability to accurately reconstruct segmentation maps.

3.3.5 Residual Skip Connection

While the base model uses skip connections to transfer feature maps directly from the encoder to the decoder, we extend this by introducing a skip connection with a residual learning mechanism (rSkip). rSkip adds the encoder’s feature maps to the decoder’s output and prevents the vanishing gradient problem. The learnable filters are then applied to the encoder feature maps. For each pair of encoder and decoder feature maps F_e and F_d , the residual connection is defined as:

$$F_{\text{residual}} = F_d + \mathcal{R}(F_e) \quad (18)$$

where \mathcal{R} represents a residual operation that applies a convolutional filter to F_e . Following this, the residual connection is

passed through a non-linear activation function to refine the feature map, as defined:

$$F_{\text{output}} = \phi(W_{\text{residual}} * F_{\text{residual}} + b_{\text{residual}}) \quad (19)$$

where $F_{\text{output}} \in \mathbb{R}^{C \times D \times H \times W}$ represents the refined feature map, while $F_{\text{residual}} \in \mathbb{R}^{C \times D \times H \times W}$ denotes the residual feature map obtained by merging decoder and encoder features. The term $W_{\text{residual}} \in \mathbb{R}^{k \times k \times k \times C}$ is the learnable convolutional filter with kernel size k , and $b_{\text{residual}} \in \mathbb{R}^C$ is the corresponding bias, with $*$ denoting convolution and $\phi(\cdot)$ as the activation function. The rSkip formulation ensures that spatial details from earlier encoding stages are preserved and refined.

3.3.6 Aggregation

Finally, we employ an aggregation strategy to combine information from multiple decoder stages before the final segmentation output. Instead of using only the highest-resolution feature map, we aggregate feature maps from multiple levels by applying a weighted summation. The aggregated feature map, $F_{\text{aggregate}}$, is defined in Equation (20) as:

$$F_{\text{aggregate}} = \sum_{l=1}^L \gamma_l F_{\text{dec}}^l \quad (20)$$

where $F_{\text{dec}}^l \in \mathbb{R}^{C_l \times D_l \times H_l \times W_l}$ represents the feature map from the l^{th} decoder stage, and γ_l are the learned scalar weights that regulate the contributions of different levels.

3.4 Classifier Architecture

The classifier architecture integrates the segmentation-based features, and the radiomics features for enhanced tumor classification, as visualized in Figure 4. We outline the initialization and finalization of feature maps through a weighted combination. Algorithm 3 summarizes the proposed classifier, with further details provided in the following sections.

3.4.1 Feature Map Initialization

Initially, we generate fused feature maps for the classifier framework by integrating two distinct sets of features: segmentation-based features derived from our model and radiomics features [Van Griethuysen et al. \(2017\)](#); [Zwanenburg et al. \(2016\)](#) extracted from the segmented output.

The segmentation model constructs spatial feature maps, F_{seg} , which capture the multi-scale spatial characteristics of the data, including both the local and global structures of the tumor region. For each voxel v in V set of voxels, the constructed feature map F_{seg} is characterized as:

$$F_{\text{seg}}(v) = [f_1(v), f_2(v), \dots, f_i(v)] \quad (21)$$

Algorithm 3 Classifier Architecture

- 1: **Input:** Segmented Volumes $V_{\text{seg}} = \{v_{\text{seg}_1}, \dots, v_{\text{seg}_n}\}$, Radiomics Features $F_{\text{rad}} = \{f_{\text{rad}_1}, \dots, f_{\text{rad}_m}\}$
 - 2: **Key Parameters:** F_{seg}^* , F_{rad}^* , F_{combined}
 - 3: **for all** $v_{\text{seg}} \in V_{\text{seg}}$ **do**
 - 4: $F_{\text{seg}}(v) \leftarrow \text{segmentation_features}(v)$
 - 5: $V_{\text{mesh}} \leftarrow \text{mesh_vol}(v_{\text{seg}})$
 - 6: $V_{\text{voxel}} \leftarrow \text{voxel_vol}(v_{\text{seg}})$
 - 7: $A_{\text{surface}} \leftarrow \text{surface_area}(v_{\text{seg}})$
 - 8: $\psi \leftarrow \text{sphericity}(v_{\text{seg}})$
 - 9: $F_{\text{seg}}^* \leftarrow \text{normalize}(F_{\text{seg}})$
 - 10: $F_{\text{rad}}^* \leftarrow \text{normalize}(V_{\text{mesh}}, V_{\text{voxel}}, A_{\text{surface}}, \psi)$
 - 11: $F_{\text{combined}} \leftarrow \alpha \cdot F_{\text{seg}}^* + \beta \cdot F_{\text{rad}}^*$
 - 12: $C_{o/p} \leftarrow \text{classifier}(F_{\text{combined}})$
 - 13: **end for**
 - 14: **Output:** Classifier Output, $C_{o/p}$
-

where $f_i(v)$ denotes the i^{th} feature extracted at voxel v . These spatial features are focused on multi-level image representations and capture patterns such as texture, intensity, and structural relationships within the segmented regions. Then, alongside the segmentation features, we include the following four radiomics features:

Mesh Volume We first utilize the segmented output to form 3D meshes by defining the boundary surface of the segmented region. Then, to calculate the mesh volume, V_{mesh} , we generate a triangular mesh from the segmented volume using a surface reconstruction algorithm. This mesh is composed of a set of vertices $\{v_i\}$, and triangular face $\{f_j\}$. The Mesh Volume is then computed as:

$$V_{\text{mesh}} = \sum_{f_j \in F} \frac{1}{6} |v_{i_1} \cdot (v_{i_2} \times v_{i_3})| \quad (22)$$

where f_j is a triangular face with vertices $v_{i_1}, v_{i_2}, v_{i_3}$; and (\cdot) and (\times) represent the dot and cross products, respectively. This equation represents the signed volume of the tetrahedron formed by the origin and the vertices of each triangular face. The sum of all faces gives the total volume enclosed by the mesh.

Voxel Volume Next, we computed the volume based on voxels, V_{voxel} , which directly sums the number of voxels classified as part of the segmented region by our model. Each voxel represents a discrete cubic volume, and the total volume is obtained by multiplying the number of segmented voxels by the volume of a single voxel, as defined:

$$V_{\text{voxel}} = n_{\text{vox}} \cdot \Delta x \cdot \Delta y \cdot \Delta z \quad (23)$$

where n_{vox} is the number of segmented voxels, and $\Delta x, \Delta y, \Delta z$ are the voxel dimensions in the x, y , and z directions, respectively.

Surface Area The Surface Area, A_{surface} , is then calculated by summing the areas of all the triangles that form the 3D

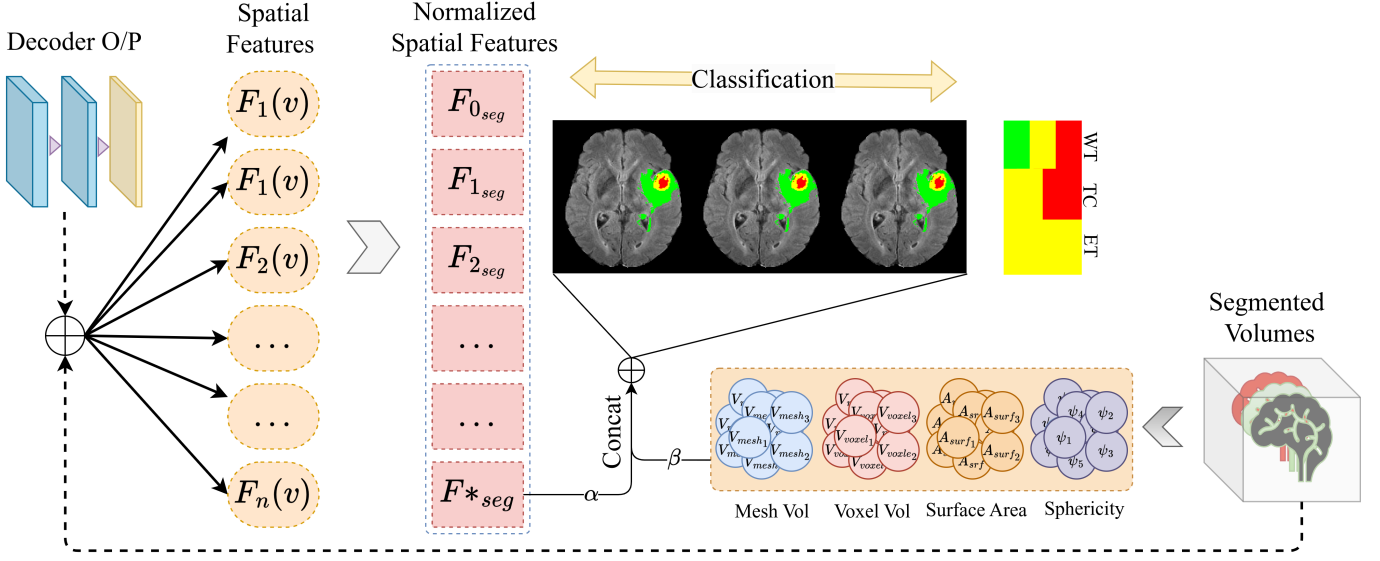


Figure 4: Overview of the proposed classifier incorporating fused maps from segmentation-based and radiomics features.

mesh. For each triangular face f_j with vertices $\{v_{i_1}, v_{i_2}, v_{i_3}\}$, the area, $A_{surface}$, is computed as:

$$A_{surface} = \sum_{f_j \in F} \frac{1}{2} |(v_{i_2} - v_{i_1}) \times (v_{i_3} - v_{i_1})| \quad (24)$$

Sphericity Finally, we calculate the Sphericity, ψ , to measure how closely the shape of the segmented region resembles a sphere. It is defined in Equation (25) as the ratio of the surface area (Eq. (24)) of a sphere with the same volume (Eq. (22)) as the region to the actual surface area of the region:

$$\psi = \frac{\pi^{\frac{1}{3}} (6V_{mesh})^{\frac{2}{3}}}{A_{surface}} \quad (25)$$

3.4.2 Feature Map Finalization

To integrate both structural characteristics from the segmentation model and shape attributes from the extracted radiomics features, we combine the feature vector from the segmentation model, F_{seg}^* , with the radiomics features, F_{rad}^* . The resulting combined feature map is then scaled to ensure consistency, as defined in Equation (26):

$$F_{combined} = \alpha \cdot F_{seg}^* + \beta \cdot F_{rad}^* \quad (26)$$

where α and β are the weighting factors that balance their respective contributions.

4 Analysis of Results

4.1 Experimental Setup

The experiments were conducted on a system configured with an AMD Ryzen 5 5600X 6-core CPU, 16 GB of RAM, and a ZOTAC RTX 3060 GPU with 12 GB of VRAM. The datasets were processed by converting the NIfTI files into .npy format. The images were resized to $128 \times 128 \times 128$ with three channels (i.e., Flair, T1ce/T1gd, and T2). A custom data generator was used to load batches of size 2, with the Adam optimizer applied at a learning rate of 0.0001. To experiment on the datasets, we utilized the predefined training, validation, and test set splits provided by the BraTS2019, BraTS2020, and BraTS2021 datasets without any further partitioning. Section 4.6 includes the detailed ablation experimental analysis with various configurations.

4.2 Training Evaluation

Two loss functions were employed while training the model to optimize performance: Dice Loss, and Categorical Focal Loss. The Dice Loss was used to address class imbalance by incorporating class weights for each tumor region. It was calculated as shown in Equation (27):

$$\mathcal{L}_{Dice} = 1 - \frac{2 \sum_{i=1}^N w_c y_i \hat{y}_i}{\sum_{i=1}^N w_c y_i + \sum_{i=1}^N w_c \hat{y}_i} \quad (27)$$

where y_i represents the ground truth binary mask, \hat{y}_i denotes the predicted mask, and w_c is the weight for class c . On the other hand, the Categorical Focal Loss was introduced to reduce the impact of hard-to-classify samples, formulated as:

$$\mathcal{L}_{Focal} = -\alpha_c (1 - p_t)^\gamma \log(p_t) \quad (28)$$

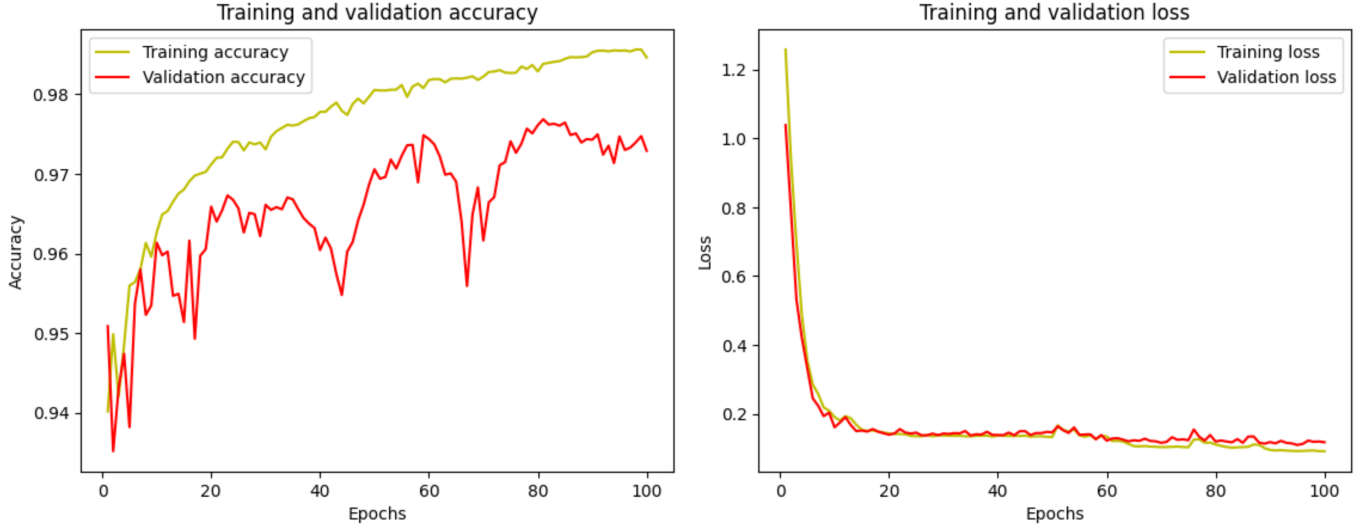


Figure 5: Epoch-wise accuracy and loss for training and validation

where α_c is the weighting factor for class c , p_t is the predicted probability for the target class, and γ is the focusing parameter to down-weight easy examples. The total loss function for our model is the summation of the two losses, as defined in Equations (27) and (28).

The model was trained on the BraTS2021 dataset due to its extensive coverage of previous and similar data modalities. After 100 epochs, the model achieved a training Dice accuracy score of 98.46% and a validation Dice accuracy score of 97.29%. The corresponding training and validation losses were 0.1032 and 0.1159, respectively. Figure 5 illustrates the accuracy and loss curves for both training and validation.

4.3 Evaluation Metrics

To evaluate the performance of our model, we employ several metrics for our multi-region tumor segmentation and classification tasks. These metrics include the Dice Similarity Coefficient (DSC), Jaccard Coefficient Score (JCS), sensitivity, and specificity. Each metric is defined to account for the multiple subregions of interest: Tumor Core (TC), Whole Tumor (WT), and Enhancing Tumor (ET).

For each subregion i , the DSC score measures the spatial overlap between the predicted segmentation A_i and the ground truth B_i , as defined in Equation (29):

$$\text{DSC}_i = \frac{2 \times |A_i \cap B_i|}{|A_i| + |B_i|}. \quad (29)$$

Next, the model’s performance is assessed using the JCS metric to calculate the average number of voxels shared by the ground truth areas over their union and the segmentation result. It is calculated as:

$$\text{JCS}_i = \frac{|A_i \cap B_i|}{|A_i \cup B_i|}. \quad (30)$$

Following this, we compute the accuracy (ACC), precision (PREC), sensitivity (SEN), and specificity (SPE) to reflect the model’s ability to correctly classify positive and negative cases. These metrics are calculated as shown in Equations (31), (32), (33), and (34):

$$\text{ACC}_i = \frac{TP_i + TN_i}{TP_i + TN_i + FP_i + FN_i}. \quad (31)$$

$$\text{PREC}_i = \frac{TP_i}{TP_i + FP_i}. \quad (32)$$

$$\text{SEN}_i = \frac{TP_i}{TP_i + FN_i}. \quad (33)$$

$$\text{SPE}_i = \frac{TN_i}{TN_i + FP_i}. \quad (34)$$

where TP_i , FP_i , TN_i , and FN_i denote true positive, false positive, true negative, and false negative, respectively, for each tumor subregion i .

In addition to these metrics, we also evaluate the model using radiomics features¹ extracted from the predicted segmented masks. Specifically, we analyze Mesh Volume, Voxel Volume, Surface Area, and Sphericity. These features are compared with the ground truth masks to gain insight into the model’s performance concerning the volumetric and geometric properties of the tumors.

¹The extracted radiomics features, as shown in Equations (22), (23), (24), and (25), are used to guide the classifier model, as detailed in Section 3.4.

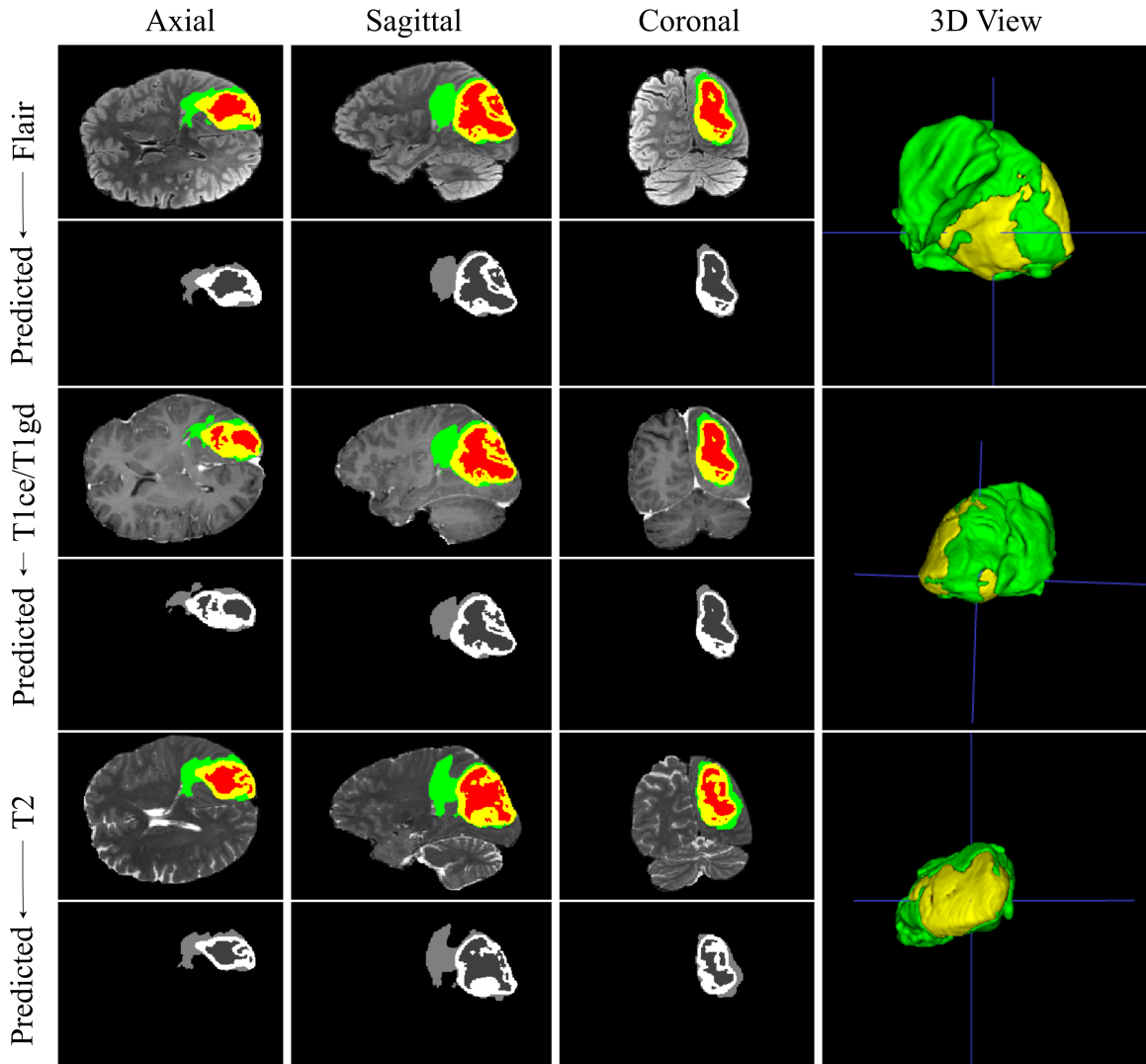


Figure 6: Predicted brain tumor segmentation across multimodal MRI (FLAIR, T1ce, T2) in axial, sagittal, and coronal views. The ITK-SNAP [Yushkevich et al. \(2006\)](#) application is used to visualize the 3D representation.

4.4 Segmentation Evaluation

The segmentation performance was evaluated using three datasets: BraTS2019, BraTS2020, and BraTS2021, across three modalities: T1ce, T2, and Flair. The Dice Similarity Coefficient (DSC) and Jaccard Coefficient Score (JCS) were used to assess the segmentation of three tumor subregions: Whole Tumor (WT), Enhancing Tumor (ET), and Tumor Core (TC).

Across all datasets, the T2 modality consistently provided higher segmentation accuracy than T1ce and Flair. In BraTS2019, the T2 modality achieved the highest DSC of 94.59%, followed by Flair (93.54%) and T1ce (92.23%). A similar trend was observed in BraTS2020, where T2 recorded 94.92% and outperformed T1ce (92.09%) and Flair (93.82%). For BraTS2021, T2 yielded the highest DSC of 92.46%, while

T1ce and Flair obtained 91.62% and 92.11%, respectively. The JCS followed a similar pattern, with T2 generally providing the best results, reaching 90.33% in BraTS2020, and the lowest observed score in T1ce for BraTS2021 (84.56%). In terms of mean values, T2 consistently achieved the highest mean DSC (94.92%) and JCS (90.33%). T1ce showed lower performance, with the lowest DSC for ET observed in BraTS2021 (89.91%) and the lowest JCS for ET at 81.67%. The best overall results were achieved in BraTS2020, where T2 outperformed the other modalities. Figure 6 illustrates the subtype prediction of the segmented tumors. Table 2 presents the detailed segmentation results for different modalities.

For BraTS2019, the model achieved a mean DSC of 93.45% and a JCS of 87.73%. The highest DSC was observed for WT (94.04%) and the lowest for ET (92.68%). Similarly,

Table 2: Segmentation results for different modalities. The columns m_m DSC and m_m JCS denote the mean Dice Similarity Coefficient and Jaccard Coefficient Similarity for the respective modalities.

| Dataset | Modalities | DSC(%) | | | m_m DSC(%) | JCS(%) | | | m_m JCS(%) |
|-----------|------------|--------|-------|-------|--------------|--------|-------|-------|--------------|
| | | WT | ET | TC | | WT | ET | TC | |
| BraTS2019 | T1ce | 92.98 | 91.17 | 92.54 | 92.23 | 86.88 | 83.77 | 85.59 | 85.59 |
| | T2 | 95.05 | 94.00 | 94.71 | 94.59 | 90.57 | 88.68 | 89.73 | 89.73 |
| | Flair | 94.10 | 92.87 | 93.66 | 93.54 | 88.86 | 86.69 | 87.88 | 87.88 |
| BraTS2020 | T1ce | 93.30 | 90.25 | 92.74 | 92.09 | 87.44 | 82.23 | 85.38 | 85.38 |
| | T2 | 94.78 | 95.08 | 94.90 | 94.92 | 90.08 | 90.62 | 90.33 | 90.33 |
| | Flair | 94.18 | 93.41 | 93.88 | 93.82 | 89.00 | 87.63 | 88.37 | 88.37 |
| BraTS2021 | T1ce | 93.01 | 89.91 | 91.93 | 91.62 | 86.93 | 81.67 | 84.56 | 84.56 |
| | T2 | 94.20 | 91.12 | 92.07 | 92.46 | 89.04 | 83.69 | 86.01 | 86.01 |
| | Flair | 93.91 | 90.05 | 92.38 | 92.11 | 88.52 | 81.90 | 85.42 | 85.42 |

the JCS ranged from 88.77% for WT to 86.38% for ET, indicating slightly lower performance for ET compared to other subregions. Table 3 details the segmentation performance on the BraTS2019 dataset.

Table 3: Comparison of segmentation performance on BraTS2019 dataset. The best results are presented in bold and the second best results are presented in underline.

| Ref | WT | ET | TC |
|----------------------------|--------------|--------------|--------------|
| Liu et al. (2023b) | 0.811 | 0.767 | 0.892 |
| Tong and Wang (2023) | 0.774 | 0.767 | 0.886 |
| Liu et al. (2023a) | 0.767 | 0.811 | 0.892 |
| Li et al. (2022) | 0.834 | 0.802 | 0.867 |
| Ullah et al. (2022) | 0.872 | 0.867 | 0.901 |
| Barzegar and Jamzad (2021) | <u>0.887</u> | <u>0.890</u> | <u>0.901</u> |
| Xu et al. (2022) | 0.820 | 0.740 | 0.900 |
| ReFRM3D (Ours) | 0.940 | 0.926 | 0.936 |

For BraTS2020, similar trends were observed, with a mean DSC of 93.61% and a JCS of 88.02%. WT recorded the highest DSC at 94.09%, while ET showed a DSC of 92.91%. The JCS values followed the same pattern, with WT scoring 88.84% and ET achieving 86.83%. As seen in Table 4, the slight increase in mean DSC and JCS from BraTS2019 to BraTS2020 indicates improved performance.

In BraTS2021, the mean DSC dropped slightly to 92.06%, and the JCS to 85.33%. WT had the highest DSC at 93.70%, while ET showed the lowest at 90.36%. As shown in Table 5, despite the reduction in performance for BraTS2021, the segmentation remained robust with DSC values above 90% for most subregions.

Table 4: Comparison of segmentation performance on BraTS2020 dataset. The best results are presented in bold and the second best results are presented in underline.

| Ref | WT | ET | TC |
|-----------------------|--------------|--------------|--------------|
| Liu et al. (2023b) | 0.817 | 0.780 | 0.883 |
| Domadia et al. (2024) | 0.769 | 0.758 | <u>0.917</u> |
| Liu et al. (2023a) | 0.780 | 0.817 | 0.883 |
| Isensee et al. (2021) | <u>0.850</u> | <u>0.820</u> | 0.895 |
| Guan et al. (2022) | 0.680 | 0.700 | 0.850 |
| Xu et al. (2022) | 0.820 | 0.780 | 0.900 |
| ReFRM3D (Ours) | 0.940 | 0.929 | 0.938 |

Table 5: Comparison of segmentation performance on BraTS2021 dataset. The best results are presented in bold and the second best results are presented in underline. Cell with N/A denotes: value not given

| Ref | WT | ET | TC |
|-----------------------|--------------|--------------|--------------|
| Domadia et al. (2024) | 0.812 | 0.758 | 0.902 |
| Sun et al. (2024) | 0.884 | N/A | 0.889 |
| Li and Guo (2024) | <u>0.911</u> | <u>0.871</u> | 0.941 |
| ReFRM3D (Ours) | 0.937 | 0.903 | <u>0.921</u> |

4.5 Classification Evaluation

In the tumor-subregion classification approach, we utilized a combination of features derived from both segmented masks and radiomic features, which were fused to enhance the classification accuracy. The features extracted from the segmented masks provided spatial information, while radiomic features provided additional volumetric and geometrical characteristics. For BraTS2019, the classification performance was

highly accurate, with WT achieving 99.7% accuracy, 99.0% precision, and 99.3% sensitivity, while ET and TC followed closely with accuracies of 99.3% and 98.8%, respectively. The specificity for all subregions remained consistently high, with values between 99.0% and 99.4%. For the BraTS2020 dataset, WT again showed strong performance with 99.4% accuracy and 99.5% precision, while ET maintained a similar performance with 99.3% accuracy and 99.1% precision. However, TC exhibited a slightly lower accuracy of 97.8%. The sensitivity for TC in BraTS2020 also dropped, to 97.1%, while the other subregions showed stable sensitivities of 98.9% and 99.7% for WT and ET, respectively. The specificity values for BraTS2020 remained near-perfect, particularly for WT and ET, at 99.8%, demonstrating the model’s capacity to avoid false positives. Lastly, in BraTS2021, the classification accuracy for WT was 99.2%, with a precision of 99.7% and sensitivity of 99.1%, indicating a marginal decrease compared to previous datasets. ET classification in BraTS2021 resulted in a slightly lower accuracy of 98.9%, but precision remained high at 99.4%, and sensitivity for ET was 98.1%. TC again presented the most challenging classification, with a 98.0% accuracy and a slight drop in sensitivity to 98.5%. Specificity for all subregions in BraTS2021 remained above 98%. Table 6 presents the averaged classification results obtained across the three leveraged datasets.

4.6 Ablation Studies

4.6.1 Experimentation on the Model Architecture

To address the challenges of glioma segmentation, particularly in capturing complex structures and maintaining high segmentation accuracy, we progressively enhanced the base 3D U-Net architecture by incorporating several key components. Initially, the base 3D U-Net provided an average DSC of 81.63%, 83.71%, and 84.97% for the BraTS2019, BraTS2020, and BraTS2021 datasets, respectively. To improve multi-scale feature representation, we introduced Fused Multi-scale Feature Fusion (FMFF), which increased the DSC to 85.90%, 87.01%, and 89.73%. This component was designed to capture features across different resolutions allowing the network to better handle the variations in tumor sizes and structures. Next, we integrated Hybrid Upsampling and Residual Integration (HURI) to refine the upsampling path and ensure better feature transitions between scales. This improvement further enhanced the model’s performance providing DSCs of 90.01%, 91.77%, and 90.91%, across the respective datasets. The Residual Skip Mechanism (rSkip) was integrated to enhance feature propagation and reduce information loss between layers, resulting in the development of the ReFRM3D model. This addition further improved the DSC, to 93.45%, 93.61%, and 92.06%. It is worth noting that the models (from base to subsequent improvement) were executed over 100 epochs at a learning rate of 0.0001 with a batch size of 2, combined with the dice and focal loss functions. Table 7 shows the detailed

Table 6: Classification results for different tumor sub-regions.

| Dataset | Accuracy (%) | | | Precision (%) | | | Sensitivity (%) | | | Specificity (%) | | | |
|-----------|--------------|------|------|---------------|------|------|-----------------|------|------|-----------------|------|------|-------|
| | WT | ET | TC | WT | ET | TC | WT | ET | TC | WT | ET | TC | Avg. |
| BraTS2019 | 99.7 | 99.3 | 98.8 | 99.0 | 99.1 | 98.4 | 99.3 | 99.8 | 98.9 | 99.4 | 99.2 | 99.0 | 99.20 |
| BraTS2020 | 99.4 | 99.3 | 97.8 | 99.5 | 99.1 | 98.2 | 98.9 | 99.7 | 97.1 | 99.8 | 99.8 | 97.0 | 99.53 |
| BraTS2021 | 99.2 | 98.9 | 98.0 | 99.7 | 99.4 | 97.7 | 99.1 | 98.1 | 98.5 | 99.4 | 99.1 | 98.7 | 99.07 |
| | | | | Avg. | | | Avg. | | | Avg. | | | |
| | | | | 99.27 | | | 99.00 | | | 99.33 | | | 99.20 |
| | | | | 98.83 | | | 99.27 | | | 98.57 | | | 99.53 |
| | | | | 98.37 | | | 99.30 | | | 98.53 | | | 99.07 |

mean Dice similarity coefficient (m_t DSC) results for different augmentations to the proposed model.

Table 7: Model components’ configuration study

| Model | m_t DSC(%) | | |
|--------------------|--------------|---------|---------|
| | BraTS19 | BraTS20 | BraTS21 |
| Base 3D UNet | 81.63 | 83.71 | 84.97 |
| Base + FMFF | 85.90 | 87.01 | 89.73 |
| Base + FMFF + HUSR | 90.01 | 91.77 | 90.91 |
| ReFRM3D (proposed) | 93.45 | 93.61 | 92.06 |

4.6.2 Hyperparameter Configurations

In this analysis of the experiments, we thoroughly examined how different configurations—image sizes, learning rates, optimizers, and loss functions—impacted the training and validation processes. The experiments were conducted over 100 epochs with a batch size of 2 for all of the configurations. Starting with image size, models trained with a smaller image size of $128 \times 128 \times 128$ generally resulted in faster convergence, as evidenced by lower training and validation loss, and higher accuracy, compared to those trained with a larger image size of $256 \times 256 \times 256$. The choice of optimizer also had a significant impact. The Adam optimizer outperformed SGD across all configurations, with Adam maintaining consistently lower training and validation losses, particularly at lower learning rates. For instance, at a learning rate of 0.0001,

Adam achieved a training accuracy of 98.2% for BraTS2019, 98.1% for BraTS2020, and 98.5% for BraTS2021, with corresponding validation accuracies above 97% for each. SGD, by contrast, showed less effective performance at higher learning rates, such as 0.01, where models experienced slower convergence and higher validation loss. The models using SGD at a learning rate of 0.01, for example, had validation accuracies as low as 90.1% on BraTS2019. Additionally, we observed that the combination of Dice Loss and Focal Loss (D&F) provided better stability and segmentation accuracy across all datasets compared to using either Dice Loss or Focal Loss alone, or the maximum of them (denoted as D/F). The D&F combination helped to handle class imbalance more effectively, particularly for small or less-represented tumor regions. This was reflected in a reduced validation loss and a higher validation accuracy, especially when paired with the Adam optimizer and lower learning rates. For instance, the BraTS2021 dataset, trained with 128^3 image dimensions, a learning rate of 0.0001, and D&F loss, achieved the highest validation accuracy of 97.3% with a validation loss of 0.116. The impact of configurations also extended to training time, where models trained with 256^3 image dimensions and SGD required more epochs to converge, thereby increasing the time per epoch. The models with larger image sizes and SGD often took more than 130 seconds per epoch on average, compared to around 120 seconds per epoch for models trained with Adam optimizer for 128^3 image dimensions. Table 8 details the parameter choices and results for this experiment.

Table 8: Hyperparameter configurations and performance metrics. The columns **LR** and **T/E (s)** represent the learning rate and the average time per epoch in seconds, respectively.

| Dataset | Size ³ | LR | Optimizer | Loss | Training | | Validation | | T/E (s) |
|-----------|-------------------|--------|-----------|------|----------|----------|------------|----------|---------|
| | | | | | Loss | Accuracy | Loss | Accuracy | |
| BraTS19 | 128 | 0.01 | Adam | D/F | 0.915 | 0.232 | 0.921 | 0.181 | 110 |
| | 128 | 0.001 | Adam | D/F | 0.955 | 0.120 | 0.969 | 0.131 | 119 |
| | 128 | 0.0001 | Adam | D&F | 0.982 | 0.110 | 0.970 | 0.120 | 125 |
| | 256 | 0.01 | SGD | D/F | 0.908 | 0.254 | 0.901 | 0.223 | 119 |
| | 256 | 0.001 | SGD | D/F | 0.961 | 0.239 | 0.947 | 0.190 | 129 |
| | 256 | 0.0001 | SGD | D&F | 0.967 | 0.193 | 0.951 | 0.157 | 137 |
| BraTS2020 | 128 | 0.01 | Adam | D/F | 0.939 | 0.200 | 0.939 | 0.171 | 108 |
| | 128 | 0.001 | Adam | D/F | 0.960 | 0.175 | 0.966 | 0.130 | 121 |
| | 128 | 0.0001 | Adam | D&F | 0.981 | 0.121 | 0.974 | 0.112 | 127 |
| | 256 | 0.01 | SGD | D/F | 0.898 | 0.229 | 0.910 | 0.199 | 125 |
| | 256 | 0.001 | SGD | D/F | 0.937 | 0.187 | 0.953 | 0.178 | 131 |
| | 256 | 0.0001 | SGD | D&F | 0.941 | 0.162 | 0.959 | 0.164 | 138 |
| BraTS2021 | 128 | 0.01 | Adam | D/F | 0.959 | 0.137 | 0.932 | 0.153 | 115 |
| | 128 | 0.001 | Adam | D/F | 0.973 | 0.128 | 0.969 | 0.120 | 121 |
| | 128 | 0.0001 | Adam | D&F | 0.985 | 0.103 | 0.973 | 0.116 | 126 |
| | 256 | 0.01 | SGD | D/F | 0.917 | 0.181 | 0.899 | 0.201 | 129 |
| | 256 | 0.001 | SGD | D/F | 0.960 | 0.167 | 0.934 | 0.173 | 134 |
| | 256 | 0.0001 | SGD | D&F | 0.967 | 0.159 | 0.944 | 0.146 | 140 |

Table 9: Effect of preprocessing techniques on model performance and efficiency.

| Preprocessing Aspect | Time/Epoch (s) | Training | | Validation | |
|---------------------------------|----------------|----------|------|------------|------|
| | | Accuracy | Loss | Accuracy | Loss |
| .nii format + w/o Preprocessing | 151±2.1 | 0.891 | 0.27 | 0.881 | 0.31 |
| .nii format + w/ Preprocessing | 135±0.9 | 0.934 | 0.25 | 0.909 | 0.26 |
| .npy format + w/o Preprocessing | 139±1.7 | 0.929 | 0.21 | 0.889 | 0.27 |
| .npy format + w/ Preprocessing | 123±2.4 | 0.944 | 0.17 | 0.917 | 0.23 |

4.6.3 Preprocessing Configurations

We experimented with the impact of our preprocessing techniques on the efficiency and performance of our segmentation model (see Section 4.1 for the experimental setup). The study was conducted on a subset of 70 samples from the BraTS2021 dataset, with training performed over 50 epochs. A learning rate of 0.0001 was used, and Dice and Focal loss functions were employed for model optimization. The preprocessing techniques included the choice of image format (.nii vs. .npy) and the methods of slice selection, both of which were applied during the preprocessing stage. Table 9 summarizes the effects of these variables on training time, accuracy, and loss.

The results show that preprocessing MRI volumes in .npy format with tumor-containing slices achieves the best performance and efficiency. Training time per epoch was reduced to 123±2.4 seconds with the .npy format after preprocessing, compared to 151±2.1 seconds for the .nii format with all slices before preprocessing. Converting to .npy format alone improved training speed, reducing epoch time from 151±2.1 seconds to 139±1.7 seconds when all slices were used before preprocessing. Preprocessing to select only tumor-containing slices further reduced epoch time.

In terms of performance, the .npy format with tumor-containing slices provided the best results: 94.4% training accuracy, 0.17 training loss, 91.7% validation accuracy, and 0.23 validation loss.

4.7 Comparison with Existing Approaches

Existing methods employ various architectural enhancements, such as multi-scale feature learning Ding et al. (2020); Zhou et al. (2020), attention mechanisms Liu et al. (2023a); Guan et al. (2022), and feature reuse modules Xue et al. (2020); Zhou et al. (2021), to improve tumor segmentation. However, these models still struggle with extracting discriminative features from multi-modal MRI data. Our approach effectively addresses these challenges by integrating optimized feature extraction and advanced multi-modal fusion.

As shown in Table 10, our model achieves superior Dice scores across all tumor subtypes segmentation. Notably, we obtain a DSC of 94.0% WT, 92.9% ET, and 93.8% TC on BraTS2020 outperforming prior works such as C-ConvNet Ranjbarzadeh et al. (2021) and ERV-Net Zhou et al. (2021),

which achieve lower scores despite employing complex network architectures. Among previous approaches, WLFS Barzegar and Jamzad (2021) performed well on BraTS2015 achieving 89.4% WT, 90.1% ET, and 91.5% TC, yet our model surpasses it across all tumor regions. Similarly, CH-UNet Xu et al. (2022) obtained 85.0% WT, 79.0% ET, and 91.0% TC on BraTS2018, demonstrating well-informed performance but still falling short of our method. C-ConvNet Ranjbarzadeh et al. (2021) achieved 91.1% ET on BraTS2018, which was among the best ET segmentations before our approach, yet our model consistently performs better across multiple datasets.

Compared to WLFS Barzegar and Jamzad (2021) and CH-UNet Xu et al. (2022), which utilize inter-slice dependencies and probabilistic frameworks, our model demonstrates enhanced segmentation consistency across tumor subregions.

5 Discussion

Our major contributions lie in the development of an optimized preprocessing pipeline, the design and enhancement of a customized 3D U-Net architecture, and the fusion of segmentation-based and radiomics features for subtype classification. Firstly, we tackled the computational inefficiency associated with 3D segmentation models, particularly in high-volume MRI datasets. In response to RQ3, we introduced a novel brain region isolation and cropping method, based on intensity thresholding and connected component analysis, which significantly reduced non-brain regions while ensuring the preservation of critical brain structures. This reduced the computational load, as evidenced in our experimental results, where the preprocessing technique using the “.npy” format and selected slices achieved the shortest training time per epoch (123±2.4 seconds) without sacrificing segmentation accuracy. This preprocessing method not only sped up training but also improved segmentation accuracy, as shown by the increase in validation accuracy to 91.7% and the corresponding drop in validation loss to 0.23. These findings highlight the importance of resource optimization in 3D medical imaging tasks, where high data volume often leads to resource exhaustion. Our ReFRM3D architecture, based on the 3D U-Net architecture, was progressively enhanced through several modifications to overcome challenges in feature representation

Table 10: Comparison of Dice (%) for different datasets and methods. The best results are highlighted in bold, while the second-best results are underlined. Studies conducted on multiple datasets are noted as "↔"

| Model | Dataset | Dice (%) | | |
|------------------------------------------|-----------|--------------|--------------|--------------|
| | | WT | ET | TC |
| DDU-net Jiang et al. (2021) | BraTS2017 | 0.838 | 0.783 | 0.898 |
| DenseNets Ding et al. (2020) | BraTS2015 | 0.816 | 0.818 | 0.858 |
| U-Net Li et al. (2019) | BraTS2015 | 0.733 | 0.726 | 0.890 |
| ↔ | BraTS2017 | 0.763 | 0.642 | 0.876 |
| C-ConvNet Ranjbarzadeh et al. (2021) | BraTS2018 | 0.872 | 0.911 | 0.920 |
| MSMANet Zhang et al. (2021b) | BraTS2018 | 0.890 | 0.758 | 0.811 |
| F 2 FCN Xue et al. (2020) | BraTS2013 | 0.780 | 0.750 | 0.880 |
| ↔ | BraTS2015 | 0.870 | 0.800 | 0.750 |
| ERV-Net Zhou et al. (2021) | BraTS2018 | 0.866 | 0.818 | 0.912 |
| DenseAFPNet Zhou et al. (2020) | BraTS2013 | 0.720 | 0.700 | 0.870 |
| ↔ | BraTS2015 | 0.700 | 0.620 | 0.830 |
| ↔ | BraTS2018 | 0.773 | 0.752 | 0.864 |
| WLFS Barzegar and Jamzad (2021) | BraTS2015 | 0.894 | 0.901 | 0.915 |
| ↔ | BraTS2017 | 0.872 | 0.886 | 0.900 |
| CH-UNet Xu et al. (2022) | BraTS2018 | 0.850 | 0.790 | 0.910 |
| 2D-CNNs Zhang et al. (2021a) | BraTS2018 | 0.850 | 0.830 | 0.820 |
| ↔ | BraTS2013 | 0.780 | 0.830 | 0.810 |
| (TS) ² WM Zhong et al. (2020) | BraTS2017 | 0.700 | 0.760 | 0.890 |
| ReFRM3D (Ours) | BraTS2019 | <u>0.940</u> | <u>0.926</u> | 0.936 |
| | BraTS2020 | 0.940 | <u>0.929</u> | 0.938 |
| | BraTS2021 | 0.937 | 0.903 | 0.921 |

and multi-scale context capture. Initially, the base 3D U-Net showed promising results but fell short in handling tumors with varying scales and shapes. To address RQ1 and RQ4, we introduced Fused Multi-scale Feature Fusion (FMFF), Hybrid Upsampling and Residual Integration (HURI), and the Residual Skip Mechanism (rSkip), which together improved multi-scale feature fusion, enhanced localization, and reduced interpolation artifacts during upsampling. These enhancements resulted in significant performance gains, as reflected in the DSC scores, which improved from 84.97% to 92.06% on the BraTS2021 dataset. The ablation study further confirmed the importance of each component, as each successive addition led to marked improvements in accuracy across multiple datasets. In response to RQ2, we developed a preprocessing technique to select the most relevant MRI slices, which reduced noise and allowed the model to focus on the essential regions containing tumors. This method improved the segmentation process by limiting unnecessary data and enhancing the model’s focus on tumor regions. We achieved a mean DSC improvement across all tumor subregions by applying this technique which proves that reducing the slice range does not compromise the model’s performance but rather improves it. To enhance tumor classification, we integrated features extracted from our segmentation model with radiomics features, such as Mesh Volume, Voxel Volume, Surface Area, and Sphericity, providing additional geometric and volumetric insight. The

combination of these features contributed to the high classification accuracy across tumor subregions (WT, ET, TC). As shown in our experimental analysis, the classification of WT consistently achieved accuracies above 99% across all datasets, while ET and TC followed closely, confirming the robustness of our classifier framework. The radiomics features, which capture tumor morphology and geometry, played a crucial role in enhancing the overall classification task, addressing RQ5. Our experimental setup and results validated the effectiveness of our model across three benchmark datasets: BraTS2019, BraTS2020, and BraTS2021. By transforming the 3D dataset format into .npy arrays for faster and more efficient training, we were able to optimize resource usage without losing information that may affect the result. The evaluation metrics, DSC, JCS, and classification accuracy, indicated that our model consistently outperformed previous approaches, with improvements, particularly in the segmentation of the WT and ET regions. Our model maintained DSC scores consistently above 90% for most tumor subregions, with the highest DSC for WT at 94.92% for BraTS2020. Finally, the ablation study demonstrated the importance of each model component. Beginning with the base 3D U-Net, we observed an initial DSC of 84.97% for BraTS2021, which improved significantly with the addition of FMFF and HURI, reaching 92.06%. Similarly, we explored the impact of different preprocessing techniques, hyperparameters, and image formats, showing that the combination of the .npy format

and selected slices was the most efficient in terms of both performance and computational time. Our study successfully addressed the challenges outlined in the research questions and provided a novel, optimized framework for glioma tumor segmentation and classification.

6 Limitations and Future Works

Despite the effectiveness of the proposed model in glioma segmentation and classification, a few limitations remain. For instance, while our framework reduces computational resource consumption and enables faster training, this efficiency is primarily attributed to our preprocessing pipeline. Additionally, our work focuses solely on brain tumor segmentation and classification relying on a supervised learning pipeline despite several novel contributions.

For future work, we aim to develop a more optimized segmentation and classification framework that extends beyond brain tumors to multiple organ types. This will involve incorporating an unsupervised learning approach to enhance adaptability and generalization across diverse medical imaging tasks.

7 Conclusion

In this paper, we developed ReFRM3D, an advanced model for glioma tumor segmentation and classification using 3D MRI data, addressing key challenges in computational efficiency, multi-scale feature extraction, and tumor morphology analysis. By enhancing the base 3D U-Net model with components such as FMFF, HURI, and rSkip, we significantly improved the segmentation accuracy across multiple tumor subregions. Additionally, our integration of radiomics features with the segmentation-based features provided a comprehensive approach to tumor classification, achieving high accuracy, particularly for complex regions like the Enhancing Tumor (ET) and Tumor Core (TC). The results from our experimental analysis, performed on the BraTS2019, BraTS2020, and BraTS2021 datasets, demonstrated that our model consistently achieved Dice Similarity Coefficients (DSC) above 90%. Moreover, our preprocessing approaches effectively reduced resource consumption while maintaining segmentation precision. The robust and efficient nature of our model makes it suitable for clinical trials.

Acknowledgment.

The authors gratefully acknowledge the financial support provided by the Institute for Advanced Research (IAR), United International University, under Project Code: UIU-IAR-02-2023-SE-23.

Declarations

Conflict of interest/Competing interests The authors declare no financial conflicts of interest or personal relationships that could have influenced this work and have consented to its publication.

Data Availability The study uses three datasets: BraTS2019², BraTS2020³, and BraTS2021⁴, all of which are publicly available.

References

- Reza Azad, Ehsan Khodapanah Aghdam, Amelie Rauland, Yiwei Jia, Atlas Haddadi Avval, Afshin Bozorgpour, Sanaz Karimijafarbigloo, Joseph Paul Cohen, Ehsan Adeli, and Dorit Merhof. Medical image segmentation review: The success of u-net. *IEEE Transactions on Pattern Analysis and Machine Intelligence*, 2024.
- Ujjwal Baid, Satyam Ghodasara, Suyash Mohan, Michel Bilello, Evan Calabrese, Errol Colak, Keyvan Farahani, Jayashree Kalpathy-Cramer, Felipe C Kitamura, Sarthak Pati, et al. The rsna-asnr-miccai brats 2021 benchmark on brain tumor segmentation and radiogenomic classification. *arXiv preprint arXiv:2107.02314*, 2021.
- Spyridon Bakas, Hamed Akbari, Aristeidis Sotiras, Michel Bilello, Martin Rozycki, Justin S Kirby, John B Freymann, Keyvan Farahani, and Christos Davatzikos. Advancing the cancer genome atlas glioma mri collections with expert segmentation labels and radiomic features. *Scientific data*, 4(1):1–13, 2017.
- Spyridon Bakas, Mauricio Reyes, Andras Jakab, Stefan Bauer, Markus Rempfler, Alessandro Crimi, Russell Takeshi Shinohara, Christoph Berger, Sung Min Ha, Martin Rozycki, et al. Identifying the best machine learning algorithms for brain tumor segmentation, progression assessment, and overall survival prediction in the brats challenge. *arXiv preprint arXiv:1811.02629*, 2018.
- Keerthiveena Balraj, Manojkumar Ramteke, Shachi Mittal, Rohit Bhargava, and Anurag S Rathore. Madr-net: multi-level attention dilated residual neural network for segmentation of medical images. *Scientific Reports*, 14(1):12699, 2024.
- Zeynab Barzegar and Mansour Jamzad. Wlfs: Weighted label fusion learning framework for glioma tumor segmentation in brain mri. *Biomedical Signal Processing and Control*, 68: 102617, 2021.
- Xu Chen, Bryan M Williams, Srinivasa R Vallabhaneni, Gabriela Czanner, Rachel Williams, and Yalin Zheng.
-
- ²<https://www.med.upenn.edu/cbica/brats2019/data.html>
- ³<https://www.med.upenn.edu/cbica/brats2020/data.html>
- ⁴<https://www.cancerimagingarchive.net/analysis-result/rsna-asnr-miccai-brats-2021/>

- Learning active contour models for medical image segmentation. In *Proceedings of the IEEE/CVF conference on computer vision and pattern recognition*, pages 11632–11640, 2019.
- Özgül Çiçek, Ahmed Abdulkadir, Soeren S Lienkamp, Thomas Brox, and Olaf Ronneberger. 3d u-net: learning dense volumetric segmentation from sparse annotation. In *Medical Image Computing and Computer-Assisted Intervention–MICCAI 2016: 19th International Conference, Athens, Greece, October 17–21, 2016, Proceedings, Part II 19*, pages 424–432. Springer, 2016.
- Tribikram Dhar, Nilanjan Dey, Surekha Borra, and R Simon Sherratt. Challenges of deep learning in medical image analysis—improving explainability and trust. *IEEE Transactions on Technology and Society*, 4(1):68–75, 2023.
- Yi Ding, Linpeng Gong, Mingfeng Zhang, Chang Li, and Zhiguang Qin. A multi-path adaptive fusion network for multimodal brain tumor segmentation. *Neurocomputing*, 412:19–30, 2020.
- Sunayana G Domadia, Falgunkumar N Thakkar, and Mayank A Ardesana. Segmenting brain glioblastoma using dense-attentive 3d daf2. *Physica Medica*, 119:103304, 2024.
- Andre Esteva, Alexandre Robicquet, Bharath Ramsundar, Volodymyr Kuleshov, Mark DePristo, Katherine Chou, Claire Cui, Greg Corrado, Sebastian Thrun, and Jeff Dean. A guide to deep learning in healthcare. *Nature medicine*, 25(1):24–29, 2019.
- K Ruwani M Fernando and Chris P Tsokos. Deep and statistical learning in biomedical imaging: State of the art in 3d mri brain tumor segmentation. *Information Fusion*, 92:450–465, 2023.
- Xi Guan, Guang Yang, Jianming Ye, Weiji Yang, Xiaomei Xu, Weiwei Jiang, and Xiaobo Lai. 3d agse-vnet: an automatic brain tumor mri data segmentation framework. *BMC medical imaging*, 22:1–18, 2022.
- Mohammad Hesam Hesamian, Wenjing Jia, Xiangjian He, and Paul Kennedy. Deep learning techniques for medical image segmentation: achievements and challenges. *Journal of digital imaging*, 32:582–596, 2019.
- Fabian Isensee, Paul F Jäger, Peter M Full, Philipp Vollmuth, and Klaus H Maier-Hein. nnu-net for brain tumor segmentation. In *Brainlesion: Glioma, Multiple Sclerosis, Stroke and Traumatic Brain Injuries: 6th International Workshop, BrainLes 2020, Held in Conjunction with MICCAI 2020, Lima, Peru, October 4, 2020, Revised Selected Papers, Part II 6*, pages 118–132. Springer, 2021.
- Min Jiang, Fuhao Zhai, and Jun Kong. A novel deep learning model ddu-net using edge features to enhance brain tumor segmentation on mr images. *Artificial Intelligence in Medicine*, 121:102180, 2021.
- Parvathy Jyothi and A Robert Singh. Deep learning models and traditional automated techniques for brain tumor segmentation in mri: a review. *Artificial intelligence review*, 56(4):2923–2969, 2023.
- Lennart R Koetzier, Domenico Mastrodicasa, Timothy P Szczykutowicz, Niels R van der Werf, Adam S Wang, Veit Sandfort, Aart J van der Molen, Dominik Fleischmann, and Martin J Willeminck. Deep learning image reconstruction for ct: technical principles and clinical prospects. *Radiology*, 306(3):e221257, 2023.
- Haichun Li, Ao Li, and Minghui Wang. A novel end-to-end brain tumor segmentation method using improved fully convolutional networks. *Computers in biology and medicine*, 108:150–160, 2019.
- Pengyu Li, Wenhao Wu, Lanxiang Liu, Fardad Michael Serry, Jinjia Wang, and Hui Han. Automatic brain tumor segmentation from multiparametric mri based on cascaded 3d u-net and 3d u-net++. *Biomedical Signal Processing and Control*, 78:103979, 2022.
- Shuai Li and Shengwen Guo. Multi-task parallel with feature sharing integrated 3d u-nets for glioma segmentation. *Biomedical Signal Processing and Control*, 93:106178, 2024.
- Hengxin Liu, Guoqiang Huo, Qiang Li, Xin Guan, and Ming-Lang Tseng. Multiscale lightweight 3d segmentation algorithm with attention mechanism: Brain tumor image segmentation. *Expert Systems with Applications*, 214:119166, 2023a.
- Xiangbin Liu, Shufen Hou, Shuai Liu, Weiping Ding, and Yudong Zhang. Attention-based multimodal glioma segmentation with multi-attention layers for small-intensity dissimilarity. *Journal of King Saud University-Computer and Information Sciences*, 35(4):183–195, 2023b.
- Maciej A Mazurowski, Haoyu Dong, Hanxue Gu, Jichen Yang, Nicholas Konz, and Yixin Zhang. Segment anything model for medical image analysis: an experimental study. *Medical Image Analysis*, 89:102918, 2023.
- Bjoern H Menze, Andras Jakab, Stefan Bauer, Jayashree Kalpathy-Cramer, Keyvan Farahani, Justin Kirby, Yuliya Burren, Nicole Porz, Johannes Slotboom, Roland Wiest, et al. The multimodal brain tumor image segmentation benchmark (brats). *IEEE transactions on medical imaging*, 34(10):1993–2024, 2014.
- Sajid Nazir, Diane M Dickson, and Muhammad Usman Akram. Survey of explainable artificial intelligence techniques for biomedical imaging with deep neural networks. *Computers in Biology and Medicine*, 156:106668, 2023.
- Quinn T Ostrom, Mackenzie Price, Corey Neff, Gino Cioffi, Kristin A Waite, Carol Kruchko, and Jill S Barnholtz-Sloan. Cbtrus statistical report: primary brain and other central nervous system tumors diagnosed in the united states in 2015–2019. *Neuro-oncology*, 24(Supplement_5):v1–v95, 2022.

- Ramin Ranjbarzadeh, Abbas Bagherian Kasgari, Saeid Jafarzadeh Ghoushchi, Shokofeh Anari, Maryam Naseri, and Malika Bendechache. Brain tumor segmentation based on deep learning and an attention mechanism using mri multi-modalities brain images. *Scientific Reports*, 11(1):1–17, 2021.
- Mohammed Salman, Pradeep Kumar Das, and Sanjay Kumar Mohanty. A systematic review on recent advancements in deep learning and mathematical modeling for efficient detection of glioblastoma. *IEEE Transactions on Instrumentation and Measurement*, 2024.
- Rebecca L Siegel, Kimberly D Miller, Nikita Sandeep Wagle, and Ahmedin Jemal. Cancer statistics, 2023. *CA: a cancer journal for clinicians*, 73(1):17–48, 2023.
- Xiangyu Sun, Sirui Li, Chao Ma, Wei Fang, Xin Jing, Chao Yang, Huan Li, Xu Zhang, Chuanbin Ge, Bo Liu, et al. Glioma subtype prediction based on radiomics of tumor and peritumoral edema under automatic segmentation. *Scientific Reports*, 14(1):27471, 2024.
- Juncheng Tong and Chunyan Wang. A dual tri-path cnn system for brain tumor segmentation. *Biomedical Signal Processing and Control*, 81:104411, 2023.
- Zahid Ullah, Muhammad Usman, Moongu Jeon, and Jeonghwan Gwak. Cascade multiscale residual attention cnns with adaptive roi for automatic brain tumor segmentation. *Information sciences*, 608:1541–1556, 2022.
- M Padma Usha, G Kannan, and M Ramamoorthy. Multi-modal brain tumor classification using convolutional turnet architecture. *Behavioural Neurology*, 2024(1):4678554, 2024.
- Joost JM Van Griethuysen, Andriy Fedorov, Chintan Parmar, Ahmed Hosny, Nicole Aucoin, Vivek Narayan, Regina GH Beets-Tan, Jean-Christophe Fillion-Robin, Steve Pieper, and Hugo JWL Aerts. Computational radiomics system to decode the radiographic phenotype. *Cancer research*, 77(21):e104–e107, 2017.
- Weijin Xu, Huihua Yang, Mingying Zhang, Zhiwei Cao, Xipeng Pan, and Wentao Liu. Brain tumor segmentation with corner attention and high-dimensional perceptual loss. *Biomedical Signal Processing and Control*, 73:103438, 2022.
- Jie Xue, Jinyan Hu, Yuan Wang, Deting Kong, Shuo Yan, Rui Zhao, Dengwang Li, Yingchao Liu, and Xiyu Liu. Hypergraph membrane system based f2 fully convolutional neural network for brain tumor segmentation. *Applied Soft Computing*, 94:106454, 2020.
- Paul A Yushkevich, Joseph Piven, Heather Cody Hazlett, Rachel Gimpel Smith, Sean Ho, James C Gee, and Guido Gerig. User-guided 3d active contour segmentation of anatomical structures: significantly improved efficiency and reliability. *Neuroimage*, 31(3):1116–1128, 2006.
- Shaoting Zhang and Dimitris Metaxas. On the challenges and perspectives of foundation models for medical image analysis. *Medical image analysis*, 91:102996, 2024.
- Xiaobing Zhang, Yin Hu, Wen Chen, Gang Huang, and Shengdong Nie. 3d brain glioma segmentation in mri through integrating multiple densely connected 2d convolutional neural networks. *Journal of Zhejiang University-SCIENCE B*, 22(6):462–475, 2021a.
- Yan Zhang, Yao Lu, Wankun Chen, Yankang Chang, Haiming Gu, and Bin Yu. Msmanet: A multi-scale mesh aggregation network for brain tumor segmentation. *Applied Soft Computing*, 110:107733, 2021b.
- Liming Zhong, Tengfei Li, Hai Shu, Chao Huang, Jason Michael Johnson, Donald F Schomer, Ho-Ling Liu, Qianjin Feng, Wei Yang, and Hongtu Zhu. 2wm: tumor segmentation and tract statistics for assessing white matter integrity with applications to glioblastoma patients. *Neuroimage*, 223:117368, 2020.
- Xinyu Zhou, Xuanya Li, Kai Hu, Yuan Zhang, Zhineng Chen, and Xieping Gao. Erv-net: An efficient 3d residual neural network for brain tumor segmentation. *Expert Systems with Applications*, 170:114566, 2021.
- Zexun Zhou, Zhongshi He, Meifeng Shi, Jinglong Du, and Dingding Chen. 3d dense connectivity network with atrous convolutional feature pyramid for brain tumor segmentation in magnetic resonance imaging of human heads. *Computers in Biology and Medicine*, 121:103766, 2020.
- Alex Zwanenburg, Stefan Leger, Martin Vallières, and Steffen Löck. Image biomarker standardisation initiative. *arXiv preprint arXiv:1612.07003*, 2016.